UNIVERSITY OF OKLAHOMA

GRADUATE COLLEGE

OPTIMIZATION AND VALIDATION OF MAIA AEROSOL RETRIEVAL USING POLDER OBSERVATIONS

A THESIS

SUBMITTED TO THE GRADUATE FACULTY

in partial fulfillment of the requirements for the

Degree of

MASTER OF SCIENCE

By

Benting Chen
Norman, Oklahoma
2024

OPTIMIZATION AND VALIDATION OF MAIA AEROSOL RETRIEVAL USING POLDER OBSERVATIONS

A THESIS APPROVED FOR THE

SCHOOL OF METEOROLOGY

BY THE COMMITTEE CONSISTING OF

Dr. Feng Xu, Chair

Dr. Jens Redemann

Dr. Lan Gao

Acknowledgment

I would like to express my gratitude to my advisor, Dr. Feng Xu, for his support and guidance throughout the three years of my master's program.

I am grateful to Dr. Lan Gao and Dr. Jens Redemann for joining my graduate committee and proofreading my thesis. I am thankful to them for providing me with valuable feedback and comments, which have helped further improve my work.

The discussion and insights from Dr. Dave Diner, Dr. Olga K. Kalashnikova, and other colleagues of JPL for this study are highly appreciated.

I want to thank all my friends who have helped and encouraged me to overcome the difficulties. Their support brought me the courage to challenge every obscurity.

This work was supported by NASA Earth Venture Instrument (EVI) Mission - Multi-angle Imager for Aerosols. The tests performed in this study used computational resources at the University of Oklahoma's (OU's) Supercomputing Center for Education & Research (OSCER).

Again, I am grateful to everyone mentioned above. Without their support and encouragement, completing this graduate thesis would not have been possible.

Table of Contents

Abstract

NASA's Multi-Angle Imager for Aerosols (MAIA) is a satellite-borne multi-angle polarimeter (MAP) instrument that aims to investigate the human health effects caused by exposures to various types of particulate matter (PM) and is anticipated to launch in 2025. The Step-1 aerosol retrieval algorithm deployed by MAIA is refined and tested by applying the algorithm to the data acquired by the satellite-borne instrument—POLarization and Directionality of the Earth's Reflectances (POLDER), and the results are compared with the ground-based Aerosol Robotic Network (AERONET) and retrieval of Generalized Retrieval of Aerosol and Surface Properties (GRASP).

To address the quilting effect observed across the edges of adjacent retrieval patches—each composed of multiple pixels that are retrieved simultaneously—a three-step strategy was implemented within the retrieval algorithm. As a significant part of this study, further advancement came with the development and integration of a neural network (NN) based radiative transfer and optics module, which has significantly accelerated the radiative transfer modeling process, increasing efficiency by three to four orders of magnitude without compromising modeling accuracy. The innovative use of automatic differentiation for the analytical Jacobian matrix calculation from the trained NNs has further accelerated computations and improved the precision of derivative estimations.

Accuracy assessments over MAIA's Los Angeles primary target area have shown that aerosol optical depth (AOD) retrievals are comparable to those from AERONET and GRASP-HP. Compared to AERONET reference AODs, the RMSEs of MAIA-NN based retrieval are 0.152, 0.050, 0.036, and 0.033 for wavelengths 565, 670, and 1020 nm, respectively. In contrast, the RMSEs of GRASP-HP based retrieval are 0.084, 0.084, 0.081, and 0.082, respectively. The three-step strategy not only mitigates the visual quality of aerosol maps but also substantially improves

retrieval performance by enforcing physically plausible constraints. As a result, there was a RMSE performance enhancement for MAIA-NN retrievals, with a notable improvement of 49%, 59%, and 62% at 565, 670, and 1020 nm wavelengths, despite a slight 4.8% decrease at 440 nm.

Remarkably, the NN-based approach has proven to be more than 400 times faster than the traditional method, taking less than 1 second per pixel on average, indicating its transformative capability for near-real-time aerosol retrieval from MAP satellite data.

List of Tables

List of Figures

1 Introduction

1.1 Background

Atmospheric aerosols are small solid or liquid particles suspended in the air ranging in size from a few nanometers to tens of micrometers. Despite their small size, they exert a notable influence on climate, air pollution, and public health. Aerosols contribute to cooling the planet by reflecting solar radiation into space, known as the direct climate effect. Additionally, tiny particles can act as cloud condensation nuclei (CCN), providing the foundation for cloud formation. This indirect influence of aerosols on climate through clouds is referred to as the indirect impact. Current research indicates that the overall climate impact of aerosols opposes that of greenhouse gas-induced warming(Haywood and Boucher, 2000; Ramanathan et al., 2001). Moreover, as a major source of air pollutants, aerosols in the boundary layer have a significant impact on human health. Fine particulate matter (PM), such as PM2.5, can penetrate deep into the respiratory system, causing respiratory diseases and cardiovascular problems. Additionally, certain aerosols (from biomass burning, industrial emissions, and engine exhaust) contain or can transport toxic chemicals exacerbating their adverse effects on human health (Pope et al., 2002).

Aerosols exhibit wide variations in terms of their sources, spatial distribution, and chemical composition. Each type of aerosol plays a distinct and critical role in shaping atmospheric processes and environmental outcomes. Understanding the complexities and nuances of aerosol properties is crucial for uncovering their broader implications for climate, air quality, and human well-being. Aerosol remote sensing provides essential constraints for these purposes.

1.2 Remote Sensing of Aerosols

One powerful tool for studying aerosols is remote sensing, which allows for the observation and measurement of aerosol properties over large spatial scales and extended periods. By

measuring and analyzing the reflected, scattered, or emitted radiation from the atmosphere, aerosol concentrations, types, and microphysical properties can be estimated.

Remote sensing instruments are deployed by various platforms, including ground-based, air-borne, and satellite-borne systems, each offering unique advantages in aerosol research. For example, the ground-based Aerosol Robotic Network (AERONET, Holben et al., 1998) utilizes instruments such as sun photometers at fixed ground stations to measure both transmitted and diffuse light and infer aerosol quantities such as aerosol optical depth (AOD), size distribution, and column abundance. Ground-based observation systems, although offering valuable long-term and accurate aerosol properties data, often face limitations in spatial coverage. In contrast, air-borne and satellite-borne instruments offer broader spatial analysis. Radiometric satellite sensors like the Moderate Resolution Imaging Spectroradiometer (MODIS, King et al., 1992; Salomonson et al., 1989) and the Multiangle Imaging SpectroRadiometer (MISR, Diner et al., 1998) have enhanced capabilities to detect aerosol properties (Kahn and Gaitley, 2015). Moreover, the integration of polarization in measurements can further improve the remote sensing accuracy of aerosol absorption (Hasekamp, 2010; Lebsock et al., 2007; Mishchenko et al., 1997). Multi-angle polarimeter (MAP) is a passive remote sensor that integrates multi-angular, multi-spectral, and polarimetric measurement abilities. Airborne Multiangle SpectroPolarimetric Imager (AirMSPI, Diner et al., 2013), for instance, is a MAP instrument that provides reliable polarimetric imaging function, seven aerosol bands from 355 to 865 nm, and high spatial resolution (10-25 meters/pixel). This and other airborne instruments like the Research Scanning Polarimeter (RSP, Cairns et al., 1999) , the airborne Spectropolarimeter for Planetary Exploration instrument (SPEX, Smit et al., 2019) and Airborne Hyper Angular Rainbow Polarimeter (AirHARP, Puthukkudy et al., 2020) have significantly advanced our measurement of aerosol properties and dynamics.

As a pioneering satellite-borne polarimeter, POLDER (Polarization and Directionality of Earth's Reflectances) has demonstrated the utility of MAP remote sensing in studying aerosol-cloud interactions, aerosol composition, and surface properties. More advanced satellite-borne MAP instruments such as Multi-viewing Multi-channel Multi-polarisation Imager (3MI, Fougnie et al., 2018) and Multi-Angle Imager for Aerosols (MAIA, Diner et al. 2018) are set to further advance the measurement capabilities to gain further insights into aerosols and their impacts.

1.3 Research Objectives and Structure

Selected by NASA's 3rd Earth Venture Instrument solicitation, the Multi-Angle Imager for Aerosols (MAIA) aims to investigate the human health effects caused by exposures to various types of particulate matter (PM) and is anticipated to launch in 2025.

To meet the scientific objectives of the MAIA project, an optimization-based aerosol inversion approach has been developed to perform the Step-1 aerosol retrieval. As the output, total/column AOD and aerosol properties including absorption, size distribution, and non-sphericity are derived and further used to calculate the AOD fractions of absorbing and non-absorbing aerosols, spherical and non-spherical aerosols, and fine and coarse mode aerosols. This study aims to validate this algorithm using POLDER data. Furthermore, considering the computationally intensive nature of the optimization-based algorithm, this research explores the integration of deep neural network (DNN) methodologies to enhance retrieval efficiency.

The upcoming chapters outline the framework and details of this structure: Chapter 2 offers a brief overview of aerosol properties, polarimetric remote sensing, surface reflection model, radiative transfer model, and the optimization-based retrieval algorithm. Chapter 3 describes the data used in this study. Chapter 4 elaborates on implementing a three-step retrieval strategy to mitigate the quilting effect of retrieved maps. Chapter 5 examines the application of DNNs in

modeling for polarimetric remote sensing. Lastly, chapter 6 summarizes the findings and discusses future research directions.

2 Radiative Transfer and Aerosol Property Inversion

2.1 Polarized Radiative Transfer Model

Radiative transfer (RT), the physical phenomenon describing the emission, absorption, and scattering of radiation, is fundamental in aerosol remote sensing. Specified for satellite remote sensing, we need to retrieve the aerosol properties from the radiance measured by satellite at the top of the atmosphere (TOA). To achieve this, a mathematical and physical model of RT must be established as a prerequisite for accurate retrieval.

To construct an effective RT module for aerosol remote sensing, it is necessary to adopt a scheme involving a coupled atmosphere-surface (CAS) system. The atmosphere system is simplified as molecule particles of gases surrounding Earth and aerosol particles. The radiance emitted and reflected by surfaces of Earth interact with the atmosphere system, also contributing an unneglectable portion of TOA radiance. A multi-layer model of the CAS system, specifically for RT modeling in this context, is detailed in Figure 2.1. Structurally, from bottom to top, the system starts with the Earth's surface, followed by a mixed layer of aerosol particles and Rayleigh scattering molecules, and capped by a pure molecule layer (Rayleigh layer).

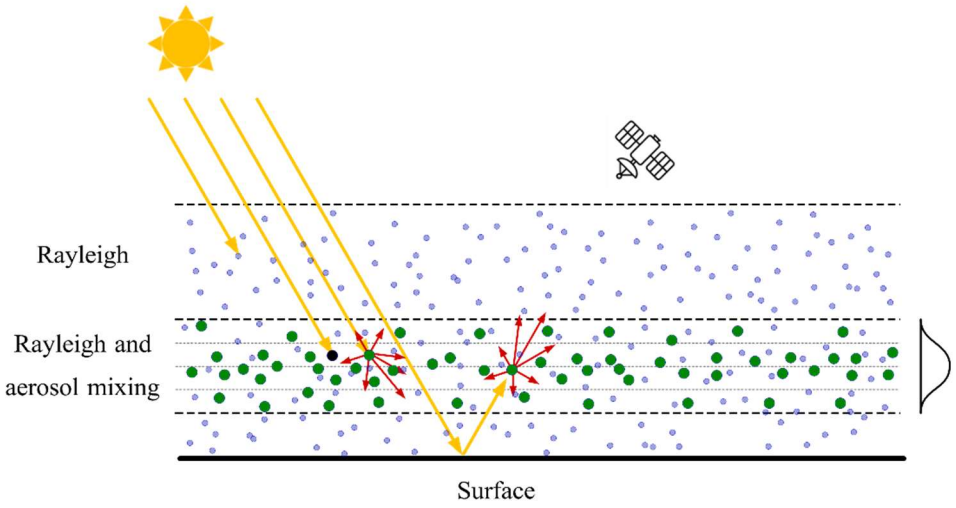

Figure 2.1 A multi-layer model of the coupled atmosphere-surface (CAS) system for RT modeling.

A hybrid Markov-chain/adding-doubling RT model (Xu et al., 2017) was adopted in the study. This model adeptly captures the complex interactions between aerosol particles and atmospheric molecules. The mixed layer above the surface is optically inhomogeneous due to the varying concentration of aerosols, and a Gaussian vertical distribution profile for aerosols is assumed. The Markov chain method is utilized for calculating polarized RT in this inhomogeneous layer, while the Rayleigh scattering layer, being optically homogeneous, uses the doubling method for RT modeling. The integration of local radiative fields across these layers, including the land surface, is achieved through an adding strategy.

The aerosol properties and surface reflectance, together with additional geometric parameters (e.g., solar and view zenith angle, solar and view azimuth angle), serve as inputs to the model. The output of this RT model includes the Stokes vector components (L, Q, U, V) of the radiance measured at the top of the CAS system. These components are then used to calculate the linear polarimetric components q and u through Eqn. (2-1) and (2-2), respectively, for fitting the signals (L, q, u) measured by a polarimetric sensor.

$$q = \frac{Q}{L} \tag{2-1}$$

$$u = \frac{U}{L} \tag{2-2}$$

2.2 Aerosol Properties

The most crucial and fundamental aerosol properties in the remote sensing field are size distribution, refractive index, and shape. They dominate the interaction of a single aerosol particle with electromagnetic radiation, such as how it absorbs and scatters the radiation in various directions.

As a proxy of aerosol composition, the complex refractive index is described as:

$$m = m_{\mathrm{r}} + m_{\mathrm{i}} i, \tag{2-3}$$

where m_{r} and m_{I} are the real and imaginary parts of the refractive index, respectively. The real part determines the extent to which light bends upon entering the interface of a particle, while the imaginary part contributes to light absorption by the particle.

Knowing the aerosol refractive index and size distribution, one can use a variety of light scattering models to compute light scattering properties from different types of particles. For example, Mie theory, a classical and purely mathematical-physical approach, describes the scattering of electromagnetic waves by homogeneous spherical particles. The T-matrix method, which extends Mie theory, offers a more efficient way to calculate scattering by non-spherical particles. The Geometric Optics Approximation (GOA) provides a simplified method for modeling light scattering by particles significantly larger than the wavelength of the incident light.

All the light scattering theories can calculate the scattering coefficient (K_{sca}), extinction coefficient (K_{ext}), and 4x4 phase matrix elements, which are used as input for radiative transfer (RT) computation.

Aerosol Optical Depth (AOD, τ) quantifies the extinction of solar or terrestrial radiation due to aerosols along the path of light propagation. It is related to the aerosol concentration and extinction coefficient (K_{ext}) by the equation:

$$\tau = \int_0^z K_{\mathrm{ext}}(z)\mathrm{d}z \tag{2-4}$$

where z is the altitude of the atmosphere.

While AOD quantifies the aerosol-induced extinction of radiation. The partial amount of reflected, absorbed, and scattered in different directions, is very important and related to particle scattering properties. Single Scattering Albedo (SSA, ϖ)

$$\varpi = \frac{K_{\text{sca}}}{K_{\text{ext}}} \tag{2-5}$$

represents the ratio of scattering to total extinction by aerosols. It is a dimensionless quantity ranging from 0 to 1. The higher the value of SSA, the stronger the scattering relative to absorption.

2.3 Surface Reflection Models

Surface reflection models describe how light is reflected from various types of surfaces (such as water, vegetation, and urban materials). As surface reflection is dependent on both the illumination and the viewing geometries, it's described as Bidirectional Reflectance Distribution Function (BRDF). For MAP instruments, both the unpolarized reflection ($\mathfrak{R}_{\text{surf,depo}}$) and polarized reflection ($\mathfrak{R}_{\text{surf,po}}$) components need to be considered, namely the overall BRDF takes the following form:

$$\mathfrak{R}_{\text{surf}} = \mathfrak{R}_{\text{surf,depo}}\mathbf{D} + \mathbf{r}(\pi - i_2)\mathfrak{R}_{\text{surf,po}}\mathbf{r}(-i_1), \tag{2-6}$$

where **D** is the null matrix except D_{11}=1, and the matrices $\mathbf{r}(\pi - i_2)$and $\mathbf{r}(-i_1)$ rotate the Stokes vector into the meridian and reflection planes via angles i_1 and i_2, respectively (Hovenier, 1969).

In this study, the Rahman-Pinty-Verstraete (RPV) model, (Rahman et al., 1993) is adopted for modeling unpolarized surface reflection components. The polarized surface reflection component is based on a micro-facet model (Cox and Munk, 1954a, 1954b; Diner et al., 2012; Litvinov et al., 2011).

2.3.1 Rahman-Pinty-Verstraete (RPV) model

The depolarizing component of BRDF as given by the RPV model (Rahman et al., 1993) is expressed as:

$$\mathfrak{R}_{\text{surf,depo}} = \frac{a_\lambda}{\pi}\frac{(\cos\theta_0 \cos\theta_{\text{v}})^{k_\lambda - 1}}{(\cos\theta_0 + \cos\theta_{\text{v}})^{1-k_\lambda}} F(g_\lambda; \Omega)[1 + R(G)], \tag{2-7}$$

where the Lambertian term $a_\lambda$controls the amplitude of reflection ($0 < a_\lambda < 1$), the modified Minnaert term k_λ dominating the bowl or bell shape of the angular distribution ($0 < k_\lambda < 1$) and g_λ is the asymmetry parameter of the Henyey-Greenstein phase function ($-1 < g_\lambda < 1$). $F(g_\lambda; \Omega)$ is evaluated as,

$$F(g_\lambda; \Omega) = \frac{1 - g_\lambda}{(1 + {g_\lambda}^2 + 2g_\lambda \cos\Omega)^{\frac{3}{2}}}. \tag{2-8}$$

The $1 + R(G)$ term in Eq. (2-7) accounts for the "hot-spot" effect, where

$$R(G) = \frac{1 - \frac{a_\lambda}{\pi}}{1 + G}, \tag{2-9}$$

and

$$G = \sqrt{\tan^2\theta_0 + \tan^2\theta_\mathrm{v} - 2\tan\theta_0 \tan|\theta_\mathrm{v}| \cos(\phi_\mathrm{v} - \phi_0)}, \tag{2-10}$$

Denoting (θ_0, ϕ_0) and (θ_v, ϕ_v) as the combinations of zenith angles and azimuthal angles of the incident and viewed light, respectively, the scattering angle is calculated by

$$\cos\Omega = -\mu_\mathrm{v}\mu_0 + \sqrt{1 - {\mu_\mathrm{v}}^2}\sqrt{1 - {\mu_0}^2}\cos(\phi_\mathrm{v} - \phi_0), \tag{2-11}$$

where μ_0 and μ_v are the cosines of θ_0 and θ_v, respectively.

2.3.2 Polarized Bidirectional Reflectance Distribution Function

The polarizing component of BRDF (pBRDF) parameters are retrieved by fitting polarimetric observations. By use of a micro-facet model (Cox and Munk, 1954a,b; Litvinov et al., 2011), the pBRDF is expressed as:

$$\Re_{\mathrm{surf,po}} = \frac{\varepsilon_\lambda}{\pi} \frac{\mathbf{F}_{\mathrm{p},\lambda}(n_\mathrm{surf}; \Omega)}{4{\mu_\mathrm{n}}^4(\cos\theta_0 + \cos\theta_\mathrm{v})} \frac{1}{2{\sigma_\mathrm{s}}^2} \exp\left(-\frac{1 - {\mu_\mathrm{n}}^2}{{\mu_\mathrm{n}}^2 2{\sigma_\mathrm{s}}^2}\right) f_\mathrm{sh}(\Omega), \tag{2-12}$$

where ε_λ controls the polarized component of the surface reflection, $\mathbf{F}_{\mathrm{p},\lambda}$ is the Fresnel reflection matrix, ${\sigma_\mathrm{s}}^2$ is the slope variance, and f_sh accounts for the shadowing effect:

$$f_\mathrm{sh}(k_\gamma; \Omega) = \left[\frac{1 + \cos k_\gamma(\pi - \Omega)}{2}\right]^3, \tag{2-13}$$

with k_γ controlling the width of the shadowing function ($0 < k_\gamma < 1$). The cosine of the tilt angle of the facet surface normal for a particular illumination and viewing geometry is given by:

$$\mu_{\mathrm{n}} = \frac{\mu_{\mathrm{v}} + \mu_0}{2} \cos^{-1}\left(\frac{\pi - \Omega}{2}\right). \tag{2-14}$$

The micro-facet model parameter ε_λ is wavelength-dependent and controls the weight of pBRDF while σ_{s} and k_γ are wavelength-independent angular shape parameters.

2.4 Optimization-based Inversion

Traditional non-polarimetric remote sensing techniques often rely on the lookup table (LUT) method due to the limited information. Hence, the LUT approach has limitations due to its reliance on discrete parameter spaces that may not capture global or temporal variations in aerosol properties, potentially leading to biased retrievals. In contrast, optimization-based retrieval methods explore solutions in a continuous parameter space, offering more flexibility and comprehensiveness. These methods maintain transparency in physics and algorithmic design and are adaptable to various observational inputs, including extra constraints to enhance retrieval accuracy. Traditional optimization techniques like Newton's method and the Levenberg-Marquardt method (Levenberg, 1944; Marquardt, 1963) have been employed in aerosol remote sensing. Nevertheless, these methods face challenges of non-uniqueness in solutions when the retrieval space is broadened to include numerous parameters with partial observational information. This issue can be partially resolved by integrating multiple observational types, such as combining lidar with polarimetric data, which enhances the information content and helps constrain the retrieval process.

The MAIA Step-1 aerosol retrieval is optimization-based and uses the multi-pixel algorithm concept (Dubovik et al., 2011). It imposes a priori smoothness conditions to constrain the spatial and temporal variations of aerosol properties and surface reflections. This approach has been

further refined by retrieving the observations acquired by MAIA's prototype instrument - the Airborne Multiangle SpectroPolarimetric Imager (AirMSPI) (Diner et al. 2013; Xu et al. 2017). Figure 2.2 illustrates the flowchart of the MAIA Step-1 aerosol retrieval algorithm used in this study.

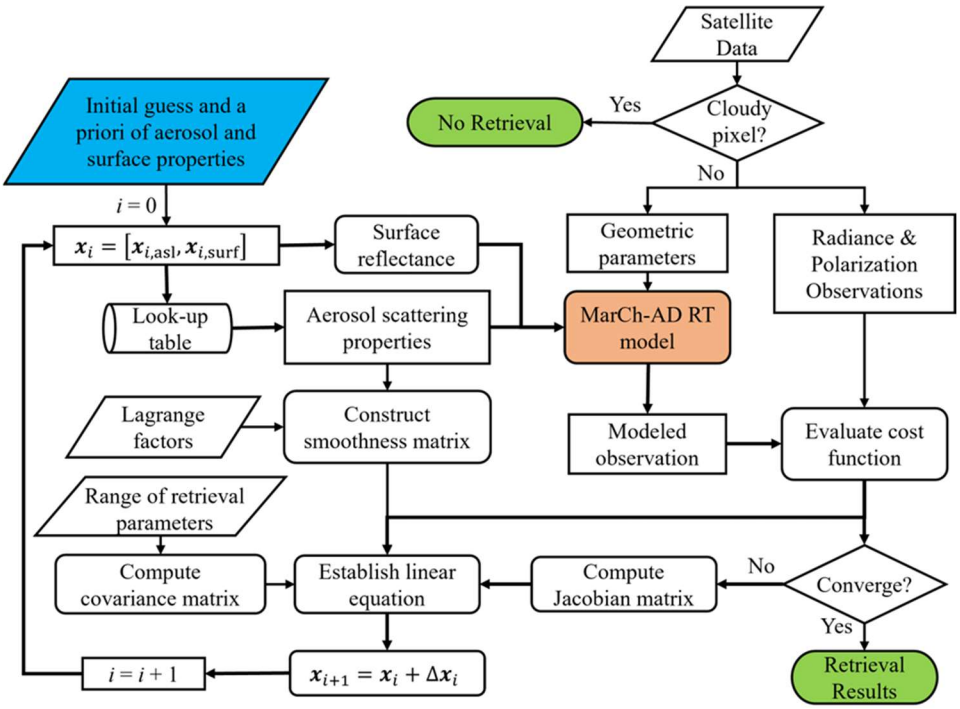

Figure 2.2 The general structure of the optimization-based aerosol and surface properties inversion algorithm.

A significant limitation of optimization-based retrieval is low efficiency due to the high computational cost of running radiative transfer modeling repeatedly to fit the measured data. Optimization is iteration-based. During these iterations, the Jacobian matrix must be computed — a process that involves individually perturbing elements of the state vector and running the forward model multiple times. To enhance the operational viability and efficiency of the optimization approach, this study integrates Deep Neural Networks (DNNs) into remote sensing modeling. The specifics of DNNs will be introduced in the chapter 5.

3 Data

To test the optimization-based MAIA Step-1 aerosol retrieval, the measurement data from multi-angle polarimeter (MAP) - POLDER is used. The purpose of this study is to check whether Step-1 retrieval can achieve similar retrieval accuracy as that of POLDER's near-real-time retrieval using the Generalized Retrieval of Atmosphere and Surface Properties (GRASP, Dubovik et al., 2010) which is also optimization-based. We will also compare the retrieval results to the ground-based AERONET reference AOD data to check the retrieval accuracy and reliability.

3.1 MAP data

3.1.1 MAIA

As a satellite-borne instrument, MAIA is anticipated to launch in 2025. Operating from space, it will focus its observations on a set of globally distributed target areas, categorized as follows:

Primary Target Areas (PTAs): These are major urban areas where MAIA's epidemiologists will investigate the effects of airborne PM on human health. Eleven PTAs have been designated for detailed study.

Secondary Target Areas (STAs): These include additional regions where the research will extend to broader air quality studies.

Calibration/Validation Target Areas (CVTAs): These areas are essential for routine observations that ensure the ongoing accuracy of the MAIA instrument's measurements and the data products derived from them.

Targets of Opportunity (TOOs): MAIA will also monitor significant episodic events, such as major wildfires or volcanic eruptions, that impact air quality. The geographic locations and frequency of observations for TOOs are flexible and event-driven.

Figure 3.2 presents the locations of the globally distributed PTAs, STAs, and CVTAs for the MAIA mission. This study's interest is focused on MAIA's PTA.

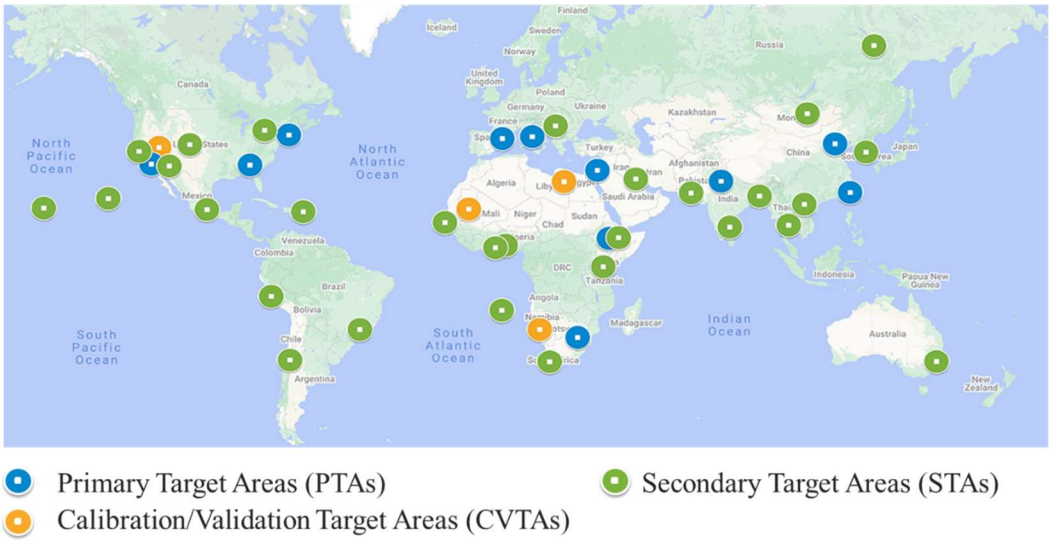

Figure 3.1 The globally distributed Primary Target Areas (PTAs), Secondary Target Areas (STAs), and Calibration/Validation Target Areas (CVTAs) locations of MAIA mission. Adapted from https://maia.jpl.nasa.gov/mission/#target_areas.

Table 1 MAIA spectral bands and their rationale.

Central Wavelength (nm)	Bandwidth (nm)	Polarization	Rationale
364	41		Aerosol absorption and height
388	40		Aerosol absorption and height
414	38		Aerosol absorption and height
440	54	Yes	Aerosol absorption and height, small aerosol size, aerosol refractive index, cloud masking
551	43		Small aerosols, surface reflection, cloud masking
646	70	Yes	Small aerosols, aerosol refractive index, cloud masking
749	18		Small aerosols, bracket absorption bands
762.5	7		Aerosol and cloud height detection
865	53	Yes	Small aerosol size, bracket absorption bands, surface reflection, cloud masking
943	47		Water vapor abundance
1044	98		Aerosol refractive index, bracket absorption bands, large aerosol size
1608	73		Large aerosols, cloud masking
1882	95		Water vapor abundance, cloud masking
2124	125		Large aerosols, surface reflection

3.1.2 POLDER

POLDER-1 and 2 flew on board the Japanese Advanced Earth Observing Satellites (ADEOS) platforms ADEOS-I and II from November 1996 to June 1997 and from April 2003 to October 2003, respectively. Unfortunately, due to the failures of the platforms' solar panels, POLDER-1

and 2 have rather a limited time series of observations. POLDER-3 was launched in December 2004 on the PARASOL (Polarization & Anisotropy of Reflectances for Atmospheric Sciences coupled with Observations from a Lidar) platform. POLDER/PARASOL (hereafter POLDER-3) was operational from March 2005 till October 2013 POLDER-3 provided global coverage about every 2 d with ~6 km spatial resolution at nadir (Tanré et al., 2011).

The POLDER-3 imager includes three gaseous absorption channels (763, 765, and 910 nm) alongside six channels (443, 490, 565, 670, 865, and 1020 nm) for measuring total radiance and three channels (490, 670, and 865 nm) for measuring polarization. The spectral bands of POLDER-3 and their purposes are detailed in Table 2. The number of viewing angles for all spectral channels ranges from 14 to 16, depending on the pixel's position on the charge-coupled device (CCD).

The Generalized Retrieval of Atmosphere and Surface Properties (GRASP) algorithm was developed to further exploit the aerosol information content of POLDER-3 spectral MAP measurements (Dubovik et al., 2011). This innovative algorithm has undergone extensive validation through systematic and/or regional case studies, affirming its reliability and accuracy on aerosol optical properties in diverse atmospheric conditions (Chen et al., 2020; Zhang et al., 2021). Hence the products of aerosol optical properties derived from GRASP from POLDER-3 MAP measurements are regarded as a crucial source of validation in this research. There are several different POLDER-3 products provided by GRASP (e.g., “optimized”, “high-precision”, and “models”). These products are consistent but were obtained using different assumptions in aerosol modeling with different accuracies of RT calculations (Chen et al., 2020). Specifically, the GRASP-HP (“high-precision”) products were utilized in this study due to their employment of the most accurate RT calculations.

Table 2 POLDER-3 spectral bands and their rationale. (Adapted from https://www.aeris-data.fr/en/projects/polder-parasol/)

Central Wavelength (nm)	Bandwidth (nm)	Polarization	Rationale
443	20		Cloud detection, ocean color
490	20	Yes	Aerosol retrieval, cloud pressure
565	20		Aerosols and Calipso lidar at 532 nm
670	20	Yes	Aerosol retrieval, cloud properties
865	20	Yes	Aerosol retrieval, cloud properties
763 and 765	40 and 10		Cloud oxygen pressure by differential absorption technique in oxygen A band
910	40		Water vapor retrieval
1020	40		Aerosols ans Calipso lidar at 1064nm

3.2 Validation Data from AERONET

AERONET products of AODs are derived from its measurements every 15 minutes. AERONET AODs can be used not only for aerosol monitoring but also as "ground truth" for validating satellite retrievals.

3.3 Data Collocation

Before implementing the validation study, we developed a method to collocate the POLDER-3 MAP measurements, the AERONET data, and GRASP aerosol property products in both temporal and spatial dimensions. The POLDER-3 measurement data are archived at the ICARE Data and Services Center, where they are organized into separate files based on different orbits. Accessing data for specific temporal and spatial requirements can be challenging due to the way the datasets are organized. We have successfully downloaded all POLDER-3 measurement data from 2005 to

2013 from https://www.icare.univ-lille.fr/asd-content/archive/?dir=PARASOL/L1_B-HDF.v1.01 and all the daily GRASP aerosol property products from https://download.grasp-sas.com/download/polder/polder-3/high-precision/v1.2/l3/.

The collocation strategy is detailed as follows:

1. Download the latitude and longitude information for all AERONET sites.
2. Identify AERONET sites within MAIA's PTAs based on the PTA geolocation range; the number of AERONET sites collocated in each PTA is listed in Table 3.
3. Determine the grid index closest to the geolocation of the collocated AERONET sites, including neighboring grid indices, as our algorithm leverages spatial information smoothness to constrain retrieval. The input to our algorithm should consist of patches of MAP measurements.
4. Iterate through all the POLDER-3 files to extract MAP measurement data from the collocated grid indices.
5. Download all AERONET data for the sites identified in step 2 and collocate this with the extracted POLDER-3 measurement data in the temporal dimension, a time difference of 45 minutes is adopted in this study.

The annual distribution of collocated cases across MAIA's 11 PTAs from 2005 to 2013 is summarized in Table 4.

Table 3 AERONET sites located within MAIA's 11 Primary Target Areas (PTAs)

Short Name of PTA	PTA Name	Number of AERONET sites
CHN	CHN-Beijing	16
ESP	ESP-Barcelona	59
ETH	ETH-AddisAbaba	2
IND	IND-Delhi	62
ISR	ISR-TelAviv	16
ITA	ITA-Rome	46
TWN	TWN-Taipei	24
USA-AT	USA-Atlanta	30
USA-BO	USA-Boston	181
USA-LA	USA-LosAngeles	77
ZAF	ZAF-Johannesburg	18

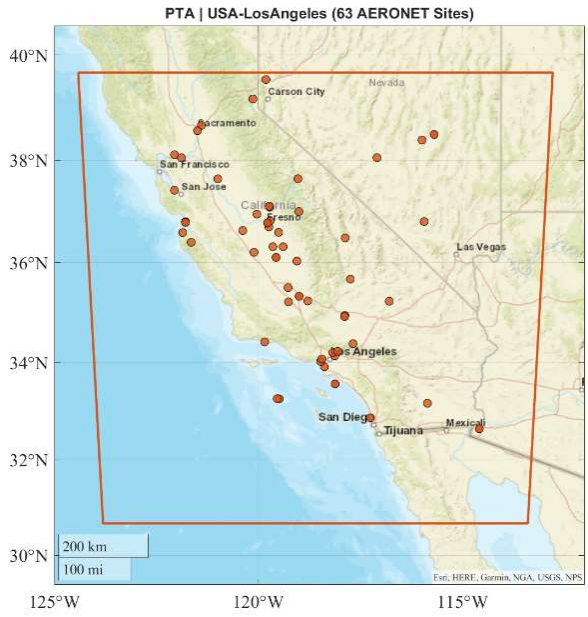

Figure 3.2 Distribution map of AERONET sites located within MAIA's USA-LosAngeles PTA.

Table 4 Annual distribution of collocated observations over MAIA's 11 PTAs from 2005 to 2013.

PTA	2005	2006	2007	2008	2009	2010	2011	2012	2013	Total
CHN	56	91	61	62	81	141	131	125	113	861
ESP	30	68	145	131	126	99	165	329	299	1392
ETH	0	0	0	0	0	0	0	0	0	0
IND	8	11	5	38	69	69	105	143	108	556
ISR	28	42	34	18	30	74	63	83	101	473
ITA	28	50	67	70	54	36	78	104	94	581
TWN	1	4	6	10	1	9	14	3	2	50
USA-AT	9	21	10	29	6	17	32	18	63	205
USA-BO	40	68	82	51	64	60	64	100	56	585
USA-LA	17	53	67	56	32	74	130	124	340	893
ZAF	6	43	34	0	36	7	37	58	6	227
Total	223	451	511	465	499	586	819	1087	1182	

4 Mitigation of Quilting Effect

Constrained by limited computer memory, the implementation of multi-pixel inversion of all pixels that compose a full MAP image at one time is not practical. To alleviate the computational burden, the retrieval process should be carried out on smaller patches, each containing a certain number ($m \times n$) of pixels. These patches can then be processed in parallel on individual computer cores. However, when retrievals are implemented on these independent patches, a quilting effect may emerge across their borders. This is due to the ill-posed nature of remote sensing inversion. Due to the lack of crosstalk across patches during the retrieval, the quilting effect is caused.

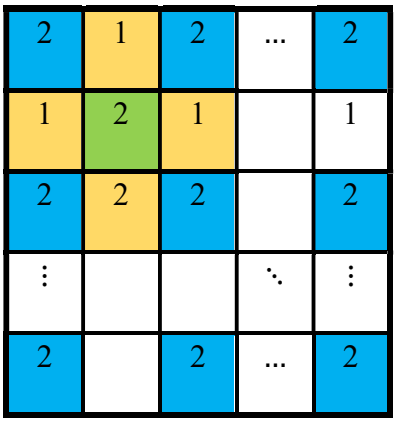

Figure 4.1 Illustration of the three-step retrieval strategy aimed at mitigating the quilting effect within a MAP observation that requires processing. The blocks marked with the numbers 1 and 2 represent distinct groups of patches, each encompassing $m \times n$ pixels.

To enable crosstalk among patches to mitigate the quilting effect, a three-step strategy is adopted as illustrated in Figure 4.1:

Step 1: Yellow patches (marked with the number 1) are retrieved in parallel.

Step 2: Blue patches (marked with the number 2) are then retrieved, with the use of Step 1 derived aerosol solutions derived at the edge pixels of the yellow patches to inform this Step-2 retrieval. Here "inform" means the use of a smoothness constraint applied to ensure the smooth transition of solution across the patch edges (Dubovik et al., 2011).

Step 3: Like Step 2 re-retrieving the blue patches again, but with the use of Step 2 derived aerosol solutions derived at the edge pixels of the yellow patches to inform this Step-3 retrieval.

The three-step retrieval strategy implemented to minimize the quilting effect is demonstrated using POLDER-3 's MAP measurements over MAIA's USA-LA PTA. The effectiveness of this approach is illustrated in the AOD map presented in Figure 4.2. Subfigure (a) shows the retrieval results across all patches without implementing the three-step strategy, where a noticeable quilting effect is observed. Subfigures (b) display the AOD outputs from applying Step 1 and Step 2 retrievals of the same POLDER-3 imagery. Subfigure (c) further includes the results from implementing all three steps of the retrieval strategy on the same imagery, demonstrating the progressive reduction of the quilting effect.

It is important to recognize that the proposed strategy not only smoothens the aerosol product maps but also significantly enhances the retrieval performance as reasonable physical constraints are imposed. As the price to pay, the three-step approach increases the computational cost by approximately 50%, thereby intensifying the demand for more efficient modeling strategies. The method to address this demand will be explored in the following chapter.

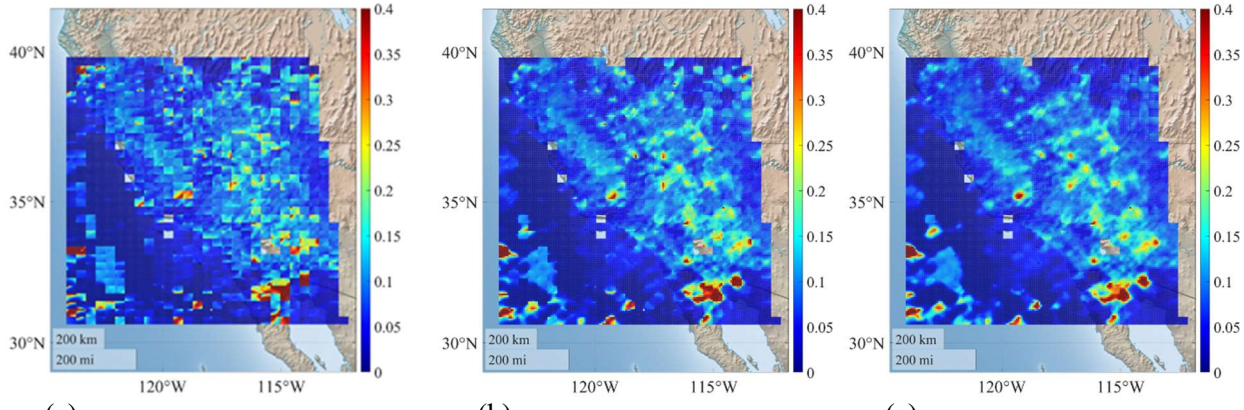

(a) (b) (c)

Figure 4.2 A demonstration of the three-step retrieval strategy designed to mitigate the quilting effect in aerosol retrieval, which is the AOD map retrieved from POLDER-3 MAP imagery over MAIA's USA-LA PTA. (a) The retrieval results over all the patches without the application of three-step strategy. (b) Output AOD from implementing Step 1 and 2 retrievals of the same POLDER-3 imagery. (c) Output AOD from implementing Step 1, 2 and 3 retrievals of the same imagery.

5 Neural Networks for Radiative Transfer Modeling

Neural network (NN) models are developing rapidly due to the advancement in machine-learning infrastructure and demands in broad applications and are demonstrated to be efficient in approximating physical functions (Lin et al., 2017).The biggest advantage that NN provides is the ability to include nonlinear terms and flexibility that are often lacking in previous deterministic or statistical approaches (Alzubaidi et al., 2021). This capability positions neural networks as a potential alternative to physical radiative transfer (RT) modeling, offering a pathway to significantly enhance computational efficiency.

5.1 Training Data

Machine learning relies on training using a large amount of data. To train an NN that can sufficiently represent the forward model for interpreting MAP measurements, we generated a large training dataset by carrying out RT simulations adopting the Markov chain radiative transfer model coupled with the adding-doubling method (Xu et al., 2016).

We simulated 1.6 million cases for each spectral band according to the forward model as discussed in section 2.4 to cover various combinations of aerosol and surface scenarios, as well as a large range of solar and viewing geometries. From these simulations, 1.5 million cases were randomly selected to be fed into the training process. These cases were divided according to the typical training, validation, and testing ratios of 0.7, 0.15, and 0.15, respectively. The remaining 0.1 million cases were set aside as test cases to assess the neural network's accuracy, which will be discussed in the next section.

To ensure comprehensive coverage of the possible range of variables, the data should be sampled from a sufficiently wide range. However, while some variables can exhibit a wide range of values, most real-world scenarios occur within a narrower range. Taking this into account, some

variables are sampled from a linear distribution, whereas others are sampled from a log-uniform distribution to better represent their actual distribution in practical scenarios. These sampling strategies are informed by climatological analyses of the variables from AERONET (if available). When the direct application of a log-uniform distribution does not align well with the climatological distributions of certain variables, we add an offset to their actual range prior to applying the log-uniform distribution. This adjustment ensures a better fit with observed data patterns. The ranges of parameters and their corresponding sampling strategies are detailed in Table 5.

Table 5 Parameters used to represent the aerosol and surface properties for the radiative transfer simulation and NN training.

Parameters	Symbol	Unit	Range	Sampling	Sampling offset
Total aerosol volume concentration	C_v	$\mu m^3/\mu m^2$	[1e-6, 5]	log-uniform	1e-2
Volume fraction of fine mode aerosols	$f_{v,\,fine}$	-	[0.01, 0.99]	Linear	-
Fine mode aerosol characteristic radius	$R_{eff,\,fine}$	μm	[0.08, 1.00]	log-uniform	0
Fine mode aerosol logarithmic characteristic width	$\ln S_{fine}$	-	[0.2, 0.6]	log-uniform	0
Coarse mode aerosol characteristic radius	$R_{eff,\,coarse}$	μm	[1, 10]	Linear	-
Coarse mode aerosol logarithmic characteristic width	$\ln S_{coarse}$	-	[0.3, 0.5]	log-uniform	0
Mean height of aerosol layer	H_{asl}	km	[0.05, 10]	log-uniform	0.5
Half width of aerosol layer	S_{asl}	km	[0.5, 2.5]	log-uniform	0
Real refractive index for fine mode aerosols	$m_{r,\,fine}$	-	[1.36, 1.60]	log-uniform	0
Imaginary refractive index for fine mode aerosols	$m_{i,\,fine}$	-	[4.9e-5, 0.1]	log-uniform	0
Real refractive index for coarse mode aerosols	$m_{r,\,coarse}$	-	[1.36, 1.60]	log-uniform	0
Imaginary refractive index for coarse mode aerosols	$m_{i,\,coarse}$	-	[4.9e-5, 0.1]	log-uniform	0
Spherical particle fraction	$f_{v,\,spheric}$	-	[0.05, 0.99]	Linear	-
Spectral weight of BRDF	a_λ	-	[1e-6, 1e-2] [1e-3, 1.001]	log-uniform	0
Anisotropy parameter 1	k_λ	-	[0.999,1.001] [1e-3, 1.001]	log-uniform	1
Anisotropy parameter 2	g_λ	-	[-0.05, 0.05] [-0.999, 0.999]	log-uniform	1
Weight of pBRDF	ε_λ	-	[0.999, 1.001] [1e-3, 50]	log-uniform	0
Shadowing width	k_γ	-	[1, 100] [1, 100]	log-uniform	0
Slope variance	σ_s^2	-	[0.01, 2π] [0.01,1]	Linear	-
Solar zenith angles	θ_0	°	[0, 75]	Linear	-
viewing zenith angles	θ_v	°	[0, 75]	Linear	-
relative viewing azimuth angle	φ_v	°	[0, 360)	Linear	-
Surface Altitude	Alt_{surf}	km	[0, 6]	log-uniform	1

5.2 Neural Network Training

A feed-forward neural network can be defined recursively with one input layer, one output layer, and *k* hidden layers:

$$\boldsymbol{h}_1 = \Phi(\boldsymbol{W}_1^{\mathrm{T}}\boldsymbol{x} + \boldsymbol{b}_1), \tag{5-1}$$

$$\boldsymbol{h}_{p+1} = \Phi\left(\boldsymbol{W}_{p+1}^{\mathrm{T}}\boldsymbol{h}_p + \boldsymbol{b}_{p+1}\right), \quad p = 1, \dots, k-1, \tag{5-2}$$

$$\boldsymbol{y} = \boldsymbol{W}_{k+1}^{\mathrm{T}}\boldsymbol{h}_k + \boldsymbol{b}_{k+1}. \tag{5-3}$$

Here for our case, $\boldsymbol{x}$ represents the input parameter vector, which includes parameters necessary for defining the forward model as outlined in Table 5, the output vector $\boldsymbol{y}$ represents predicted Multi-Angle Polarization (MAP) measurements by the neural network, and Φ is the activation function. The weight matrix $\boldsymbol{W}_{p+1}$ and bias vector $\boldsymbol{b}_{p+1}$ facilitate connections between the *p*th and (*p*+1)th NN layers via Eq. (5-2). Figure 5.1 illustrates the schematic structure of a neural network mode for estimating polarimetric radiance.

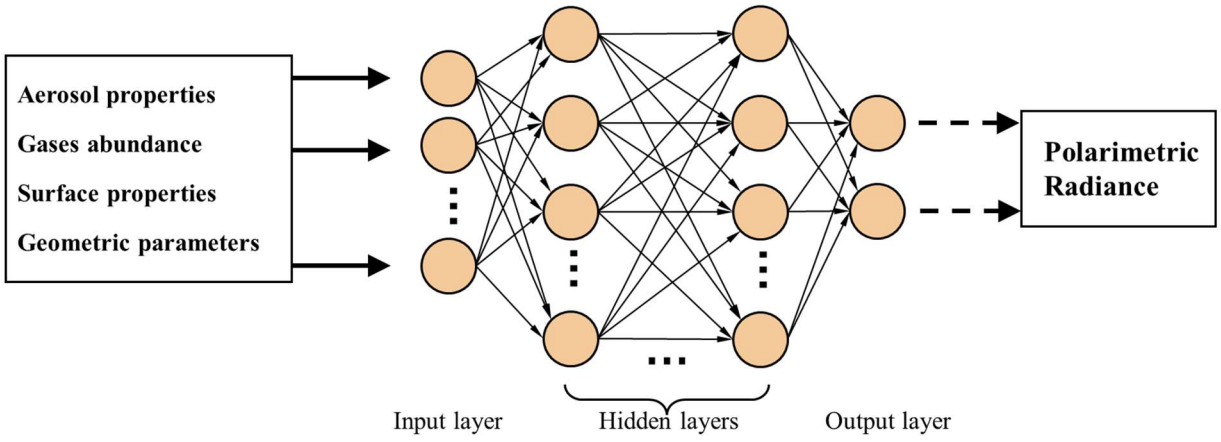

Figure 5.1 Schematic diagram of a neural network mode for estimating polarimetric radiance. The left box indicates the input parameters including aerosol properties, gases abundance, surface reflection properties, and geometric parameters.

Various activation functions were evaluated, and the hyperbolic tangent (Tanh) function was chosen for the hidden layers due to its smooth, nonlinear characteristics that are conducive to

regression tasks. The Tanh function is frequently employed in situations requiring nuanced nonlinearity, which is defined as:

$$\tanh(x) = \frac{e^{x} - e^{-x}}{e^{x} + e^{-x}}. \tag{5-4}$$

After conducting plenty of tests on the training settings, the neural network architecture configurations are finalized as 3 hidden layers with 18 neurons each for aerosol optical properties (AOD and SSA); for τ_{mixed}, which combines AOD and Rayleigh scattering-induced extinction, the NN architectures are 4 hidden layers and 18 neurons per layer; for the MAP measurements (BRF, q, and u), the architecture involved 7 hidden layers with 18 neurons each.

The training process aims to minimize the cost function, defined here as the mean square error (MSE) between the training data generated from radiative transfer simulations and the predicted NN values. The selection of hyperparameters and architecture requires careful optimization. In this study, the Levenberg-Marquardt (LM) algorithm was employed as the optimizer, providing efficient optimization during the backpropagation step. Overall, the optimization of the models can be summarized in four steps:

1. Compute the output vector $\boldsymbol{y}$ from the input vector $\boldsymbol{x}$ through the hidden layers.
2. Calculate the mean squared error (MSE) cost function using the given truth.
3. Employ the LM algorithm in the backward propagation step to update the parameters.
4. Iteratively update the weights until the optimal solution is achieved.

5.3 Accuracy Assessment

We evaluate the training accuracy of NN-based optics and RT models using 0.1 million simulation cases that have not been used in the training. Figure 5.2 presents a side-by-side evaluation of the neural network predictions and direct computational results of optical properties AOD and SSA, RT quantities including intensity (or radiance, expressed in BRF units), and the

polarimetric component q at the 440 nm POLDER-3 band. Figure 5.3 outlines the mean absolute error (MAE) over a land surface for (a) L, (b) q, (c) u, (d) AOD, and (e) SSA. The associated error bars denote the standard deviation. While there is some variability, the neural network model demonstrates reasonable performance of accuracy, especially in predicting BRF, AOD, and SSA. This study underscores the feasibility of replacing the online/physical optics and RT model with the use of NN optics and RT model.

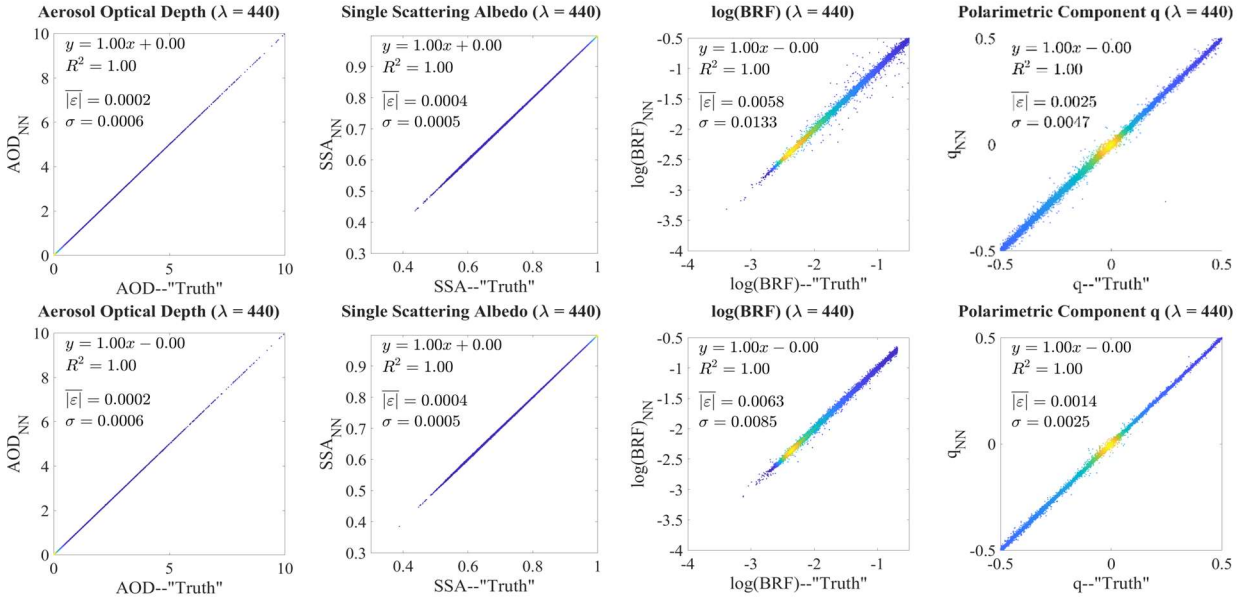

Figure 5.2 Comparison of neural-network and direct calculations of AOD, SSA, intensity (in BRF unit) and polarimetric component q at 440 nm band.

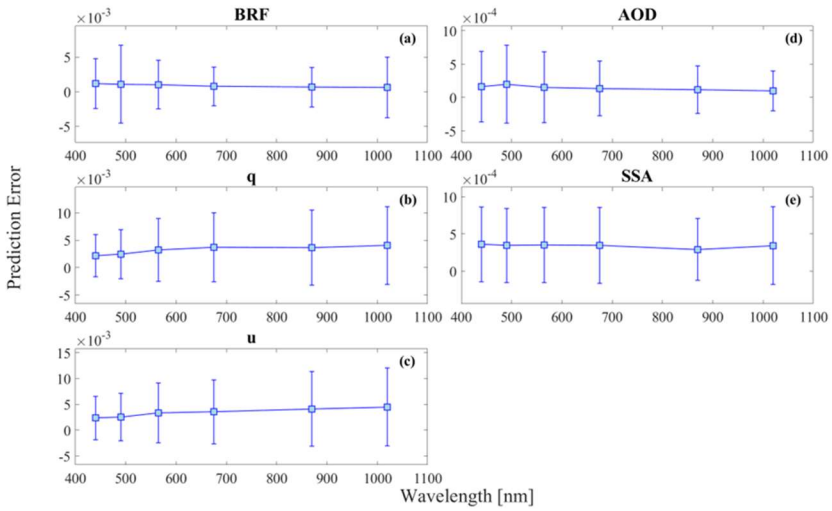

Figure 5.3 Prediction error profiles for POLDER-3 band measurements over land surface, showing Mean Absolute Error (MAE) for (a) Bidirectional Reflectance Factor (BRF), (b) linear polarization components q, (c) linear polarization components u, (d) Aerosol Optical Depth (AOD), and (e) Single Scattering Albedo (SSA), with standard deviations represented by error bars.

To enhance the accuracy of NNs, the inclusion of more training data and the development of more complex network architectures could be beneficial. In this case, however, the LM optimizer deployed by DNN will require more memory and a longer time for Jacobian matrix (with respect to network weights) evaluation. The latter is computationally intensive for large networks. The optimizer used in the current study would not be suitable for further improvement. A more viable alternative for scaling up could be the Adaptive Moment Estimation (Adam) optimizer. The algorithm has been shown to perform well in practice and converges rapidly for large datasets and/or large-scale machine-learning problems (Kingma and Ba, 2017).

5.4 Jacobian Matrix

As described in the chapter 2.4, one of the drawbacks of the optimization-based retrieval method is Jacobian matrix needs to be calculated, which involves repeatedly calling forward radiative transfer if Jacobian calculation uses a finite difference method (FDM).

The Jacobian matrix is pivotal in optimization-based retrieval. It describes how radiative quantities respond to small perturbations in the state vector components. It is required at the iterative step to guide the direction and magnitude of steps to take to move toward a convergent solution. For an observation vector comprising N measurements ($y = [y_1, y_2, \dots, y_N]^{\mathrm{T}}$) and a state vector of M components ($x = [x_1, x_2, \dots, x_M]^{\mathrm{T}}$), the Jacobian matrix exhibits the following structure,

$$\mathbf{J} = \begin{bmatrix} \frac{\partial y_1}{\partial x_1} & \frac{\partial y_1}{\partial x_2} & \cdots & \frac{\partial y_1}{\partial x_M} \\ \frac{\partial y_2}{\partial x_1} & \frac{\partial y_2}{\partial x_2} & \cdots & \frac{\partial y_2}{\partial x_M} \\ \vdots & \vdots & \ddots & \vdots \\ \frac{\partial y_N}{\partial x_1} & \frac{\partial y_N}{\partial x_2} & \cdots & \frac{\partial y_N}{\partial x_M} \end{bmatrix}_{N \times M}. \tag{5-5}$$

Each matrix element within the Jacobian matrix needs to be calculated utilizing FDM,

$$\frac{\partial y_n}{\partial x_m} = \frac{y_n(x_1, x_2, \dots, (x_m + \Delta x_m), \cdots x_M) - y_n(x_1, x_2, \dots, x_m, \cdots x_M)}{\Delta x_m}. \tag{5-6}$$

In our case, state vectors typically have a length of 23, whereas POLDER-3 measurements typically with a length of 180 (comprising 12 radiance and polarization measurements across 15 angles each). This means that the neural networks need to be invoked 8280 times to calculate the Jacobian for a single set of state vectors at each iteration step. Despite the rapid computational capability of neural networks, this still places an extreme computational burden on the retrieval process.

To mitigate this issue and further accelerate the retrieval speed, we employ a strategy of deriving the Jacobian matrix analytically from the neural network model instead of using FDM. This approach is based on automatic differentiation techniques, which utilize the chain rule of calculus to compute derivatives quickly and accurately, allowing for the efficient calculation of

gradients even in complex neural networks (Baydin et al., 2018). By applying the chain rule to the neural networks layer by layer, the Jacobian matrix can be expressed as follows:

$$\begin{cases} \dfrac{\partial h_1}{\partial x_m} & = W_{1,m} \dfrac{\partial \Phi}{\partial x_m} \\ \dfrac{\partial h_{p+1}}{\partial x_m} & = W_{p+1,m} \dfrac{\partial h_p}{\partial x_m} \dfrac{\partial \Phi}{\partial x_m} \quad (k=1,2,\cdots,k-1). \\ \dfrac{\partial y_n}{\partial x_m} & = W_{k+1,m} \dfrac{\partial h_k}{\partial x_m} \dfrac{\partial \Phi}{\partial x_m} \end{cases} \tag{5-7}$$

It should be noted that the chosen activation function Φ must be differentiable to ensure that Equation (5-7) is valid.

The method not only speeds up the computation by avoiding the computationally expensive process of calculating derivatives via finite differences but also increases the accuracy of the derivative estimates, which are crucial for iteration-based optimization processes. By analytically computing the Jacobian matrix directly from the neural network outputs, we substantially reduce the number of neural network evaluations required per iteration, thereby accelerating the overall retrieval process without sacrificing accuracy.

5.5 Joint Retrieval Results on POLDER-3 MAP Data

Following the successful development of NN-RT and NN-optics models, they are integrated into the MAIA's Level 2 aerosol retrieval algorithm. The efficacy of the NN-enhanced MAIA aerosol retrieval algorithm (hereafter MAIA-NN) is evaluated using the collocated POLDER-3 MAP data spanning from 2008 to 2011 over MAIA’s USA-LA PTA, encompassing a total of 287 scenarios. The performance of MAIA-NN is compared against the physical online RT-based MAIA aerosol retrieval algorithm (hereafter MAIA-OL), as well as reference data obtained from ground-based AERONET measurements and GRASP-HP (High-Precision daily products v1.2) retrievals.

All three aerosol retrieval algorithms: GRASP-HP, MAIA-OL, and MAIA-NN are compared against AERONET reference data at the four POLDER-3 aerosol bands shared with AERONET (440, 675, 870, and 1020 nm). For quantifying the validation results, we used standard statistical parameters, including slope and bias of linear regression, Pearson's linear correlation coefficient (R), and root-mean-square error (RMSE). The metrics of R and RMSE are calculated as follows:

$$R = \frac{\sum_{i=1}^{N}((x_{i,\text{retreval}} - \overline{x_{\text{retrıeval}}})((x_{i,\text{AERONET}} - \overline{x_{\text{AERONET}}})}{\sqrt{\sum_{i=1}^{N}(x_{i,\text{retreval}} - \overline{x_{\text{retrıeval}}})^2 \sum_{i=1}^{N}(x_{i,\text{AERONET}} - \overline{x_{\text{AERONET}}})^2}}, \tag{5-8}$$

$$\text{RMSE} = \sqrt{\frac{\sum_{i=1}^{N}(x_{i,\text{retreval}} - x_{i,\text{AERONET}})^2}{N}}. \tag{5-9}$$

Figure 5.4 shows the comparison of MAIA-OL and GRASP-HP retrievals of AODs against AERONET reference data. Figure 5.5 shows the comparison of MAIA-NN and GRASP-HP retrievals of AODs against AERONET reference data. The comparative analysis of slope and bias metrics across the algorithms is detailed in Table 6, while the analysis of R and RMSE can be found in

Table 7.

It should be noted that in both Table 6 and Table 7, the metrics displayed for MAIA-OL retrievals pertain exclusively to Step-3 of the three-step strategy. In contrast, for MAIA-NN, metrics for both Step-1 as well as Step-3 retrievals are included.

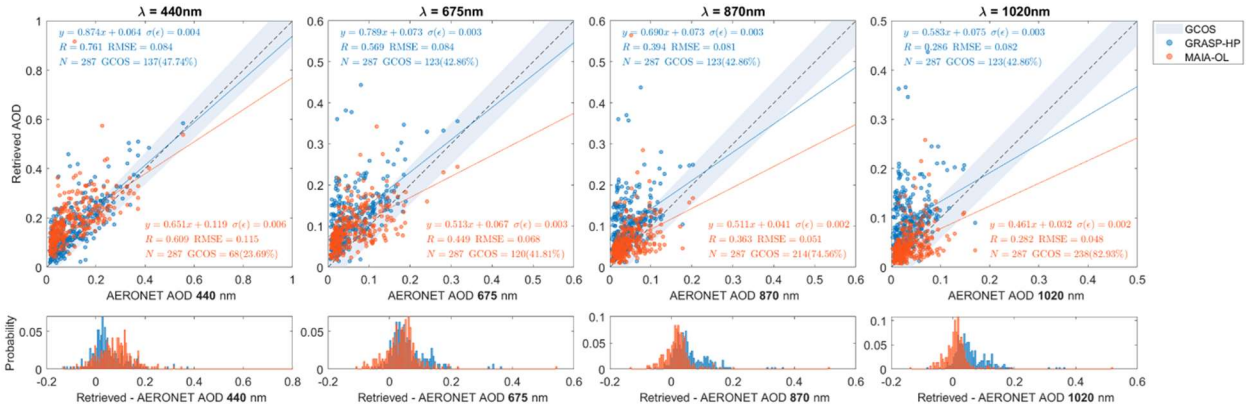

Figure 5.4 Comparison of MAIA-OL based retrieval of AODs to GRASP retrievals and to AERONET reference AODs at the four POLDER-3 aerosol bands shared with AERONET.

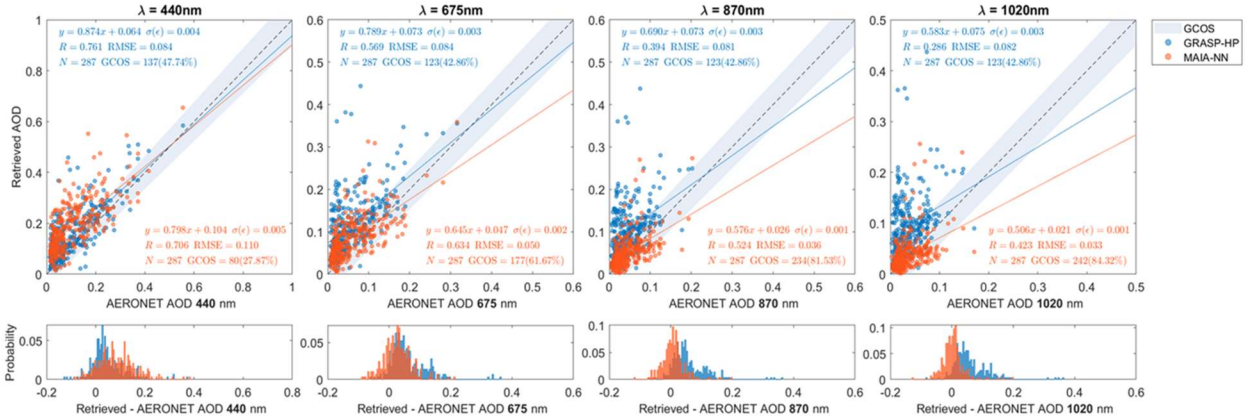

Figure 5.5 Same as Figure 5.4 but for MAIA-NN based retrieval.

Table 6 Comparison of aerosol retrieval algorithm performance on AOD at the four POLDER-3 aerosol bands shared with AERONET: slope and bias metrics for GRASP-HP, MAIA-OL, and MAIA-NN algorithms.

Algorithm	440 nm		675 nm		870 nm		1020 nm	
	Slope	Intercept	Slope	Intercept	Slope	Intercept	Slope	Intercept
GRASP-HP	0.874	0.064	0.789	0.073	0.690	0.073	0.583	0.075
MAIA-OL	0.651	0.119	0.513	0.067	0.511	0.041	0.461	0.032
MAIA-NN Step-1	0.851	0.108	0.651	0.062	0.563	0.044	0.465	0.039
MAIA-NN Step-3	0.798	0.104	0.645	0.047	0.576	0.026	0.506	0.021

Table 7 Similar with Table 6, but for R and RMSE metrics.

Algorithm	440 nm		675 nm		870 nm		1020 nm	
	R	RMSE	R	RMSE	R	RMSE	R	RMSE
GRASP-HP	0.761	0.084	0.569	0.084	0.394	0.081	0.286	0.082
MAIA-OL	0.609	0.115	0.449	0.068	0.363	0.051	0.282	0.048
MAIA-NN Step-1	0.559	0.145	0.353	0.098	0.226	0.088	0.155	0.087
MAIA-NN Step-3	0.706	0.152	0.634	0.050	0.524	0.036	0.423	0.033

Generally, both MAIA-OL and MAIA-NN show comparable performance with GRASP-HP. Specifically, at the 440 nm wavelength, GRASP-HP demonstrates superior statistical performance in comparison to AERONET reference AODs. GRASP-HP achieves a slope closest to 1 (0.874), which is better than MAIA-OL (0.651) and MAIA-NN (0.798). Additionally, GRASP-HP exhibits a higher correlation coefficient (R = 0.761) and lower values of bias (0.064) and RMSE (0.084) compared to MAIA-OL (R = 0.609, bias = 0.119, RMSE = 0.115) and MAIA-NN (R = 0.706, bias

= 0.104, RMSE = 0.152). At other bands, both MAIA-OL and MAIA-NN show an overall lower bias and RMSE compared to GRASP-HP, suggesting a closer match to the reference data. For example, at the band of 675 nm, the bias and RMSE values of GRASP-HP are 0.073 and 0.084 respectively, while those metrics for both MAIA-OL (bias = 0.067, RMSE = 0.068) and MAIA-NN (bias = 0.047, RMSE = 0.050).

The introduction of the three-step strategy aimed at reducing the quilting effect has resulted in overall enhanced performance across the bands. Although with a slight decrease of about 4.8% at 440 nm indicating a performance drop, improvements were observed at other wavelengths, specifically approximately enhancements of 49%, 59%, and 62% for 565, 670, and 1020 nm, respectively.

In comparing the two MAIA methods, MAIA-OL and MAIA-NN exhibit similar scatter patterns when compared with AERONET data, signifying the effectiveness of using neural networks to approximate the physical RT model. Statistically, MAIA-NN seems to excel beyond MAIA-OL, likely due to the efficiency of deriving the Jacobian matrix directly from the neural network outputs.

All three aerosol retrievals show some spread around AERONET reference data, which could be due to a) screening residue of cloud contamination at some view angles; and b) modeling bias from using the RPV surface reflection model. Given the information "budget" offered by POLDER-3, optimization over a large number of retrieval parameters increases the diversity of the solution to fit observation. In this case, extra a priori constraints are needed to further constrain retrieval, and retrieval parameters need to be down-selected.

A notable advancement in computational efficiency is achieved through the application of DNNs for RT modeling in aerosol property retrievals. In an assessment of 287 cases, where each

case comprises five 3×3-pixel patches, MAIA-OL's processing time totaled around 660 hours, averaging roughly 2.3 hours per case. In contrast, the MAIA-NN algorithm reduced the overall computational time to about 1.57 hours, with the average per-case duration dropping to approximately 0.006 hours, less than 20 seconds. This efficiency leap, over 400 times, underscores the significant potential of DNNs to boost the speed and scalability of near-real-time aerosol retrievals from MAP satellite data.

6 Summary and Outlook

In this study, we extensively tested the MAIA Step-1 aerosol retrieval component using POLDER-3 MAP data. Aerosol retrievals over MAIA's USA-LA PTA demonstrate the AOD accuracy comparable to that of GRASP-HP retrieval of POLDER-3 data.

To overcome the quilting effect observed at the junctions of retrieval patches, a novel three-step strategy was implemented. It not only smoothens the aerosol product maps but also significantly enhances the retrieval performance as physically realistic constraints are imposed, and further smooths the inherent ill-posed problem in remote sensing retrieval. The advancements were quantitatively evident, with RMSE improvements for MAIA-NN retrievals at 49%, 59%, and 62% for wavelengths of 565, 670, and 1020 nm respectively, despite a minor reduction of 4.8% at 440 nm.

Significant advancements were made by integrating an NN-based module for radiative transfer and optics. This integration also included the use of automatic differentiation for calculating the analytical Jacobian matrix, speeding up computations, and improving the precision of derivative estimations. What's more, probability due to the precise analytical Jacobian matrix calculations, the statistical metrics vailed an overall superior performance of MAIA-NN compared to the physical-based MAIA-OL algorithm.

Building on the advancements described, accuracy assessments carried out over 287 cases in MAIA's USA-LA PTA from 2008 to 2011 revealed that AOD retrievals are comparable to those from AERONET and GRASP-HP. Compared to AERONET reference AODs, the RMSE of MAIA-NN based retrieval are 0.152, 0.050, 0.036, and 0.033 for wavelengths 440, 565, 670, and 1020 nm, respectively. In contrast, the RMSE values for GRASP-HP based retrieval were 0.084, 0.084, 0.081, and 0.082 for the same wavelengths, respectively.

It should be noted that though MAIA Step-1 aerosol retrieval accuracy is comparable to that of near-real GRASP retrieval when retrieving POLDER-3 data, it still does not meet MAIA's AOD uncertainty target, which is the maximum of either 0.05 or 15% for column AODs in the mid-visible range. This shortfall highlights several issues:

1. The limitation of POLDER-3 spectral measurements across visible to near-infrared spectral range and its measurement uncertainty (2% relative to the magnitude of radiance and 0.01 for the degree of linear polarization, as noted by Dubovik et al., 2011) impact the high AOD retrieval accuracy.
2. The necessity of imposing further a priori constraints (e.g. a priori of surface reflection and aerosol properties) into the optimization of retrieval processes.
3. The need to further advance both the forward and inversion models to enhance retrieval accuracy.

With MAIA's broader spectral coverage, extending from ultraviolet to shortwave infrared, and its higher polarimetric measurement accuracy (e.g., 0.5% for the degree of linear polarization), improvements are anticipated. The integration of the following strategies is expected to bolster AOD retrieval accuracy:

1. Utilizing estimated AODs from Step-0 retrieval, which is based on MISR’s look-up table search approach (Kahn et al., 2010);
2. Incorporating a priori knowledge of surface reflection from the MAIAC surface dataset (Lyapustin et al., 2018) into the aerosol characterization.

Adopting such strategies has already shown promising results in column AOD retrieval using MISR data over MAIA's USA-LA PTA, where targeted MAIA AOD retrieval accuracies have

been achieved (Wenzhi Zhang, private communication). Based on these successes, further retrieval tests are planned at additional MAIA PTAs at the next stage.

7 References

Alzubaidi, L., Zhang, J., Humaidi, A.J., Al-Dujaili, A., Duan, Y., Al-Shamma, O., Santamaría, J., Fadhel, M.A., Al-Amidie, M., Farhan, L., 2021. Review of deep learning: concepts, CNN architectures, challenges, applications, future directions. J. Big Data 8, 53. https://doi.org/10.1186/s40537-021-00444-8

Baydin, A.G., Pearlmutter, B.A., Radul, A.A., Siskind, J.M., 2018. Automatic Differentiation in Machine Learning: a Survey. J. Mach. Learn. Res.

Cairns, B., Russell, E.E., Travis, L.D., 1999. The Research Scanning Polarimeter: Calibration and Ground-based Measurements. Proc. SPIE 3754, 186. https://doi.org/10.1117/12.366329

Chen, C., Dubovik, O., Fuertes, D., Litvinov, P., Lapyonok, T., Lopatin, A., Ducos, F., Derimian, Y., Herman, M., Tanré, D., Remer, L.A., Lyapustin, A., Sayer, A.M., Levy, R.C., Hsu, N.C., Descloitres, J., Li, L., Torres, B., Karol, Y., Herrera, M., Herreras, M., Aspetsberger, M., Wanzenboeck, M., Bindreiter, L., Marth, D., Hangler, A., Federspiel, C., 2020. Validation of GRASP algorithm product from POLDER/PARASOL data and assessment of multi-angular polarimetry potential for aerosol monitoring. Earth Syst. Sci. Data 12, 3573–3620. https://doi.org/10.5194/essd-12-3573-2020

Cox, C., Munk, W., 1954a. Statistics of the sea surface derived from sun glitter. J. Opt. Soc. Am. 44, 838–850.

Cox, C., Munk, W., 1954b. Measurement of the Roughness of the Sea Surface from Photographs of the Sun's Glitter. JOSA 44, 838–850. https://doi.org/10.1364/JOSA.44.000838

Diner, D.J., Beckert, J.C., Reilly, T.H., Bruegge, C.J., Conel, J.E., Kahn, R.A., Martonchik, J.V., Ackerman, T.P., Davies, R., Gerstl, S.A.W., Gordon, H.R., Muller, J., Myneni, R.B., Sellers, P.J., Pinty, B., Verstraete, M.M., 1998. Multi-angle Imaging SpectroRadiometer

(MISR) instrument description and experiment overview. IEEE Trans. Geosci. Remote Sens. 36, 1072–1087. https://doi.org/10.1109/36.700992

Diner, D.J., Boland, S.W., Brauer, M., Bruegge, C., Burke, K.A., Chipman, R., Di Girolamo, L., Garay, M.J., Hasheminassab, S., Hyer, E., 2018. Advances in multiangle satellite remote sensing of speciated airborne particulate matter and association with adverse health effects: from MISR to MAIA. J. Appl. Remote Sens. 12, 1. https://doi.org/10.1117/1.JRS.12.042603

Diner, D.J., Xu, F., Garay, M.J., Martonchik, J.V., Rheingans, B.E., Geier, S., Davis, A., Hancock, B.R., Jovanovic, V.M., Bull, M.A., Capraro, K., Chipman, R.A., McClain, S.C., 2013. The Airborne Multiangle SpectroPolarimetric Imager (AirMSPI): a new tool for aerosol and cloud remote sensing. Atmospheric Meas. Tech. 6, 2007–2025. https://doi.org/10.5194/amt-6-2007-2013

Diner, D.J., Xu, F., Martonchik, J., Rheingans, B., Geier, S., Jovanovic, V., Davis, A., Chipman, R., McClain, S., 2012. Exploration of a Polarized Surface Bidirectional Reflectance Model Using the Ground-Based Multiangle SpectroPolarimetric Imager. Atmosphere 3, 591–619. https://doi.org/10.3390/atmos3040591

Dubovik, O., Herman, M., Holdak, A., Lapyonok, T., Tanré, D., Deuzé, J.L., Ducos, F., Sinyuk, A., Lopatin, A., 2011. Statistically optimized inversion algorithm for enhanced retrieval of aerosol properties from spectral multi-angle polarimetric satellite observations. Atmospheric Meas. Tech. 4, 975–1018. https://doi.org/10.5194/amt-4-975-2011

Fougnie, B., Marbach, T., Lacan, A., Lang, R., Schlüssel, P., Poli, G., Munro, R., Couto, A.B., 2018. The multi-viewing multi-channel multi-polarisation imager – Overview of the 3MI

polarimetric mission for aerosol and cloud characterization. J. Quant. Spectrosc. Radiat. Transf. 219, 23–32. https://doi.org/10.1016/j.jqsrt.2018.07.008

Hasekamp, O.P., 2010. Capability of multi-viewing-angle photo-polarimetric measurements for the simultaneous retrieval of aerosol and cloud properties. Atmospheric Meas. Tech. 3, 839–851. https://doi.org/10.5194/amt-3-839-2010

Haywood, J., Boucher, O., 2000. Estimates of the direct and indirect radiative forcing due to tropospheric aerosols: A review. Rev. Geophys. 38, 513–543. https://doi.org/10.1029/1999RG000078

Holben, B.N., Eck, T.F., Slutsker, I., Tanré, D., Buis, J.P., Setzer, A., Vermote, E., Reagan, J.A., Kaufman, Y.J., Nakajima, T., Lavenu, F., Jankowiak, I., Smirnov, A., 1998. AERONET—A Federated Instrument Network and Data Archive for Aerosol Characterization. Remote Sens. Environ. 66, 1–16. https://doi.org/10.1016/S0034-4257(98)00031-5

Hovenier, J.W., 1969. Symmetry Relationships for Scattering of Polarized Light in a Slab of Randomly Oriented Particles. J. Atmospheric Sci. 26, 488–499. https://doi.org/10.1175/1520-0469(1969)026<0488:SRFSOP>2.0.CO;2

Kahn, R.A., Gaitley, B.J., 2015. An analysis of global aerosol type as retrieved by MISR. J. Geophys. Res. Atmospheres 120, 4248–4281. https://doi.org/10.1002/2015JD023322

Kahn, R.A., Gaitley, B.J., Garay, M.J., Diner, D.J., Eck, T.F., Smirnov, A., Holben, B.N., 2010. Multiangle Imaging SpectroRadiometer global aerosol product assessment by comparison with the Aerosol Robotic Network. J. Geophys. Res. Atmospheres 115. https://doi.org/10.1029/2010JD014601

King, M.D., Kaufman, Y.J., Menzel, W.P., Tanre, D., 1992. Remote sensing of cloud, aerosol, and water vapor properties from the moderate resolution imaging spectrometer (MODIS). IEEE Trans. Geosci. Remote Sens. 30, 2–27. https://doi.org/10.1109/36.124212

Kingma, D.P., Ba, J., 2017. Adam: A Method for Stochastic Optimization.

Lebsock, M.D., L'Ecuyer, T.S., Stephens, G.L., 2007. Information content of near-infrared spaceborne multiangular polarization measurements for aerosol retrievals. J. Geophys. Res. Atmospheres 112, 2007JD008535. https://doi.org/10.1029/2007JD008535

Levenberg, K., 1944. A method for the solution of certain non-linear problems in least squares. Q. Appl. Math. 2, 164–168. https://doi.org/10.1090/qam/10666

Lin, H.W., Tegmark, M., Rolnick, D., 2017. Why Does Deep and Cheap Learning Work So Well? J. Stat. Phys. 168, 1223–1247. https://doi.org/10.1007/s10955-017-1836-5

Litvinov, P., Hasekamp, O., Cairns, B., 2011. Models for surface reflection of radiance and polarized radiance: Comparison with airborne multi-angle photopolarimetric measurements and implications for modeling top-of-atmosphere measurements. Remote Sens. Environ. 115, 781–792. https://doi.org/10.1016/j.rse.2010.11.005

Lyapustin, A., Wang, Y., Korkin, S., Huang, D., 2018. MODIS Collection 6 MAIAC algorithm. Atmospheric Meas. Tech. 11, 5741–5765. https://doi.org/10.5194/amt-11-5741-2018

Marquardt, D.W., 1963. An Algorithm for Least-Squares Estimation of Nonlinear Parameters. J. Soc. Ind. Appl. Math. 11, 431–441. https://doi.org/10.1137/0111030

Mishchenko, M.I., Travis, L.D., Kahn, R.A., West, R.A., 1997. Modeling phase functions for dustlike tropospheric aerosols using a shape mixture of randomly oriented polydisperse spheroids. J. Geophys. Res. Atmospheres 102, 16831–16847. https://doi.org/10.1029/96JD02110

Pope, C.A., Richard, B., Michael, T., Eugenia, C., Daniel, K., Kazuhiko, I., George, T., 2002. Lung Cancer, Cardiopulmonary Mortality, and Long-term Exposure to Fine Particulate Air Pollution. JAMA 287, 1132. https://doi.org/10.1001/jama.287.9.1132

Puthukkudy, A., Martins, J.V., Remer, L.A., Xu, X., Dubovik, O., Litvinov, P., McBride, B., Burton, S., Barbosa, H.M.J., 2020. Retrieval of aerosol properties from Airborne Hyper AngularRainbow Polarimeter (AirHARP) observations during ACEPOL 2017. https://doi.org/10.5194/amt-2020-64

Rahman, H., Pinty, B., Verstraete, M.M., 1993. Coupled surface-atmosphere reflectance (CSAR) model: 2. Semiempirical surface model usable with NOAA advanced very high resolution radiometer data. J. Geophys. Res. Atmospheres 98, 20791–20801. https://doi.org/10.1029/93JD02072

Ramanathan, V., Crutzen, P.J., Kiehl, J.T., Rosenfeld, D., 2001. Aerosols, Climate, and the Hydrological Cycle. Science 294, 2119–2124. https://doi.org/10.1126/science.1064034

Salomonson, V.V., Barnes, W.L., Maymon, P.W., Montgomery, H.E., Ostrow, H., 1989. MODIS: advanced facility instrument for studies of the Earth as a system. IEEE Trans. Geosci. Remote Sens. 27, 145–153. https://doi.org/10.1109/36.20292

Smit, J.M., Rietjens, J.H.H., Harten, G. van, Noia, A.D., Laauwen, W., Rheingans, B.E., Diner, D.J., Cairns, B., Wasilewski, A., Knobelspiesse, K.D., Ferrare, R., Hasekamp, O.P., 2019. SPEX airborne spectropolarimeter calibration and performance. Appl. Opt. 58, 5695–5719. https://doi.org/10.1364/AO.58.005695

Tanré, D., Bréon, F.M., Deuzé, J.L., Dubovik, O., Ducos, F., François, P., Goloub, P., Herman, M., Lifermann, A., Waquet, F., 2011. Remote sensing of aerosols by using polarized,

directional and spectral measurements within the A-Train: the PARASOL mission. Atmospheric Meas. Tech. 4, 1383–1395. https://doi.org/10.5194/amt-4-1383-2011

Xu, F., Dubovik, O., Zhai, P.-W., Diner, D.J., Kalashnikova, O.V., Seidel, F.C., Litvinov, P., Bovchaliuk, A., Garay, M.J., Van Harten, G., Davis, A.B., 2016. Joint retrieval of aerosol and water-leaving radiance frommultispectral, multiangular and polarimetric measurements over ocean. Atmospheric Meas. Tech. 9, 2877–2907. https://doi.org/10.5194/amt-9-2877-2016

Xu, F., van Harten, G., Diner, D.J., Kalashnikova, O.V., Seidel, F.C., Bruegge, C.J., Dubovik, O., 2017. Coupled retrieval of aerosol properties and land surface reflection using the Airborne Multiangle SpectroPolarimetric Imager. J. Geophys. Res. Atmospheres 122, 7004–7026. https://doi.org/10.1002/2017JD026776

Zhang, X., Li, L., Chen, C., Chen, X., Dubovik, O., Derimian, Y., Gui, K., Zheng, Y., Zhao, H., Zhang, L., Guo, B., Wang, Y., Holben, B., Che, H., Zhang, X., 2021. Validation of the aerosol optical property products derived by the GRASP/Component approach from multi-angular polarimetric observations. Atmospheric Res. 263, 105802. https://doi.org/10.1016/j.atmosres.2021.105802